Metal Oxide Electrocatalyst Support for Carbon-free Durable Electrodes with Excellent Corrosion Resistance at High Potential Conditions

Journal:	*Sustainable Energy & Fuels*
Manuscript ID	SE-COM-09-2020-001295.R1
Article Type:	Communication
Date Submitted by the Author:	02-Feb-2021
Complete List of Authors:	Sugawara, Yuuki; Tokyo Institute of Technology, Laboratory for Chemistry and Life Science Hihara, Takuya; Tokyo Institute of Technology, Laboratory for Chemistry and Life Science Gopinathan, Anilkumar; Noritake Co Ltd, Research and Development Kamata, Keigo; Tokyo Institute of Technology, Laboratory for Materials and Structures Laboratory, Institute of Innovative Research Yamaguchi, Takeo; Tokyo Institute of Technology, Laboratory for Chemistry and Life Science

SCHOLARONE™
Manuscripts

COMMUNICATION

Metal Oxide Electrocatalyst Support for Carbon-free Durable Electrodes with Excellent Corrosion Resistance at High Potential Conditions

Yuuki Sugawara,[a] Takuya Hihara,[a] Gopinathan M. Anilkumar,[ab] Keigo Kamata[c] and Takeo Yamaguchi*[a]

Ti_2O_3 was used as a corrosion-resistive catalyst support for electrocatalytic reactions at high potential conditions. The model electrocatalyst/Ti_2O_3 electrode, BSCF/Ti_2O_3, demonstrated a considerably higher durability than a carbon support at a highly oxidative potential and completely retained its OER performance after 2000 repeated potential cycles. Therefore, Ti_2O_3 is promising as a conductive support for electrochemical catalytic reactions at high potential conditions.

Metal oxides have been used in various applications, such as superconductors,[1–3] photovoltaics,[4,5] ferrites,[6,7] and catalysts,[8–13] because of their thermal, electronic, magnetic, and chemical characteristics. Recently, the electronically conducting properties of metal oxides have received considerable attention because the current energy issues have prompted the development of electrochemical devices for energy conversion and storage such as fuel cells and lithium-ion batteries. In the electrodes of such electrochemical devices, carbon materials are typically used as conductive supports for electrocatalysts.[14,15] These carbon materials have high electronic conductivity, which enhances electron transport from active sites on catalysts to the electrodes during an electrocatalytic reaction. However, the use of carbon materials at high anodic potentials in, *e.g.*, oxygen evolution reaction (OER), is discouraged because the high potential causes carbon corrosion and deterioration of electrochemical performance.[16] Although graphitized carbons, such as carbon nanotubes (CNTs) and graphenes, exhibit slower corrosion rates than carbon black,[17] the corrosion resistance of graphitized carbon remains insufficient.

Therefore, alternative materials for conductive supports are required; thus, several conductive metal oxides have recently attracted considerable interest. For example, titanium oxides,[18,19] antimony-doped tin oxides,[20] and tungsten oxides[21] have been applied as conductive support with electrocatalysts for water electrolysis and fuel cells. Among these metal oxides, substoichiometric titanium oxides are promising because of their high electronic conductivity, excellent stability both in acidic and alkaline conditions, and prominent resistance for electrochemical corrosion at high potential. Although Ti_4O_7 and doped TiO_2 have been exploited as conductive supports for electrocatalysts, few studies use Ti_2O_3 as a conductive support. Ti_2O_3 is a semiconducting compound with good electronic conductivity[22] and shows good thermodynamic stability with high melting point (>1800 °C).[23] Conductive Ti_2O_3, such as ENETIA® series, has been recently studied on supports with electrocatalysts for CO_2 electroreduction and fuel cell cathodes.[24] However, the applicability of Ti_2O_3 as a conductive support for electrocatalysis at oxidative potentials has never been studied.

In the present study, we demonstrate the excellent durability of Ti_2O_3 as a conductive support for electrocatalysts of OER in alkaline media to evaluate the corrosion resistance of Ti_2O_3 at high potential conditions and its superiority to carbon support. We selected a benchmark nonprecious metal-based OER electrocatalyst, $Ba_{0.5}Sr_{0.5}Co_{0.8}Fe_{0.2}O_{3-\delta}$ (BSCF), as a model electrocatalyst, and BSCF was supported on ENETIA® Ti_2O_3 *via* annealing in an inert atmosphere, which is denoted as BSCF/Ti_2O_3, as shown in Fig. 1. Then, the durability of BSCF/Ti_2O_3 is evaluated by repeated potential cycles at the high potential for OER and compared with that of a graphitized carbon support[25] with relatively better corrosion resistivity, *i.e.*, CNT.
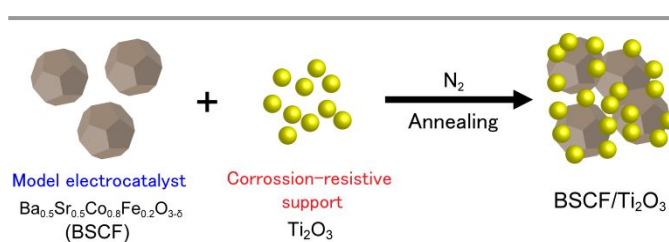
[a.] *Laboratory for Chemistry and Life Science, Institute of Innovative Research, Tokyo Institute of Technology, Nagatsuta-cho 4259, Midori-ku, Yokohama 226-8503, Japan.*
[b.] *R&D Centre, Noritake Company LTD, 300 Higashiyama, Miyoshi, Aichi 470-0293, Japan.*
[c.] *Laboratory for Materials and Structures, Institute of Innovative Research, Tokyo Institute of Technology, Nagatsuta-cho 4259, Midori-ku, Yokohama 226-8503, Japan.*

Fig. 1 Schematic of BSCF/Ti_2O_3 and its fabrication scheme.

BSCF was synthesized *via* the aspartic acid-aided sol–gel method.[26] The details of synthetic procedures are provided in ESI. The powder X-ray diffraction (XRD) pattern for BSCF was consistent with that for the previously reported orthorhombic BSCF phase [space group: Pnma] (Fig. S3).[27] The crystallite diameter was calculated to be 103 nm by Scherrer's equation. The Brunauer–Emmett–Teller (BET) specific surface area of BSCF was 9 $m^2\ g^{-1}$. Subsequently, BSCF/Ti_2O_3 was fabricated by annealing of the powder mixture of BSCF and Ti_2O_3 in a N_2 atmosphere. Fig. 2a displays the XRD pattern of BSCF/Ti_2O_3 with weight composition of 50% BSCF after annealing at 800 °C, which is denoted as 50BSCF/Ti_2O_3_800. The XRD pattern shows diffraction peaks corresponding to BSCF; however, diffraction peaks of Ti_2O_3 were not detected. Instead, the diffraction peaks of tetragonal rutile-type TiO_2 were observed. To further examine the effect of the annealing process, we annealed the mixture of BSCF and Ti_2O_3 at different temperatures. Fig. S4 exhibited the XRD patterns of 50BSCF/Ti_2O_3 after annealing at 200, 400, 600, and 800 °C, which are denoted as 50BSCF/Ti_2O_3_200, 50BSCF/Ti_2O_3_400, 50BSCF/Ti_2O_3_600, and 50BSCF/Ti_2O_3_800, respectively. The clear peaks of Ti_2O_3 were detected only for 50BSCF/Ti_2O_3_200. The diffraction peaks of both Ti_2O_3 and TiO_2 appeared for 50BSCF/Ti_2O_3_400. The diffraction peaks of TiO_2 intensified with an increase in annealing temperature. This result suggested that Ti_2O_3 was oxidized by annealing at higher temperatures and transformed into TiO_2. Basically, such oxidization does not occur during annealing in a N_2 atmosphere. However, in the case of BSCF/Ti_2O_3, oxygen was supplied by BSCF, which was suggested by the peak shifts in XRD patterns of 50BSCF/Ti_2O_3 samples compared with those of pristine BSCF, as shown in Fig. S5. In addition, 50BSCF/Ti_2O_3_800 was also analyzed by UV-vis spectroscopy, which demonstrated that characteristic absorption of Ti_2O_3 disappeared after the annealing with BSCF, but a similar absorption to TiO_2 was observed (Fig. S6). To determine the oxidized support, we analyzed bonding environments in BSCF/Ti_2O_3 by Raman spectroscopy. The Raman spectra in Fig. S7 in ESI show that the peak of the O–Ti–O symmetric stretching vibration band at 420 cm^{-1} in BSCF/Ti_2O_3 samples shifted compared with that of pristine TiO_2. This band shift is typically triggered by the presence of oxygen vacancy in TiO_2.[28] These results indicate that BSCF/Ti_2O_3 is composed of $TiO_{2-\delta}$ as the titanium oxide support after annealing at 400, 600, and 800 °C; notably, $TiO_{2-\delta}$ possesses a much higher electric conductivity than stoichiometric TiO_2.[29] Fig. 2b shows scanning electron microscopy (SEM) image of 50BSCF/Ti_2O_3_800, which demonstrates that $TiO_{2-\delta}$ nanoparticles were attached to BSCF particles. Additionally, the BET specific surface area of 50BSCF/Ti_2O_3_800 was 8 $m^2\ g^{-1}$, which was slightly smaller than that of pristine BSCF, which implied the adhesion of grain boundary between BSCF and Ti_2O_3 particles. Fig. 2c shows high-resolution transmission electron microscopy (HR-TEM) images of 50BSCF/Ti_2O_3_800, which highlight the fringes with the *d*-spacing of 0.28 and 0.32 nm, which are associated with the (121) plane of BSCF and the (110) plane of $TiO_{2-\delta}$, respectively. Furthermore, Fig. 2d shows the scanning TEM (STEM)-energy-dispersive X-ray (EDX) images on

the cross-sections of sample particles of 50BSCF/Ti_2O_3_800. The EDX elemental mapping demonstrates that $TiO_{2-\delta}$ and BSCF nanoparticles were still separately present after annealing. Moreover, Fig. S8 shows the XRD pattern of 50BSCF/Ti_2O_3 after annealing at 1000 °C, which is denoted as 50BSCF/Ti_2O_3_1000. The XRD pattern indicates the generation of multiple new phases by annealing, such as $Ba_4Ti_{11}O_{26}$ and $Ba_{1.3}Co_{1.3}Ti_{6.7}O_{16}$. The new phases were caused by unexpected reactions between BSCF and Ti_2O_3 particles. Thus, annealing at 1000 °C is unfavourable condition for the fabrication of 50BSCF/Ti_2O_3.

The OER activities of fabricated BSCF/Ti_2O_3 samples were evaluated using a typical three-electrode system with a rotating disk electrode (RDE). The details of electrochemical measurements are described in ESI. Fig. 3a shows the *iR*-corrected OER polarization curves of 50BSCF/Ti_2O_3_800, physically mixed BSCF and Ti_2O_3 with 50 wt% BSCF without annealing (denoted as 50BSCF/Ti_2O_3_PM), annealed BSCF at 800 °C without Ti_2O_3 (denoted as BSCF_800), and annealed Ti_2O_3 at 800 °C without BSCF (denoted as Ti_2O_3_800). The polarization
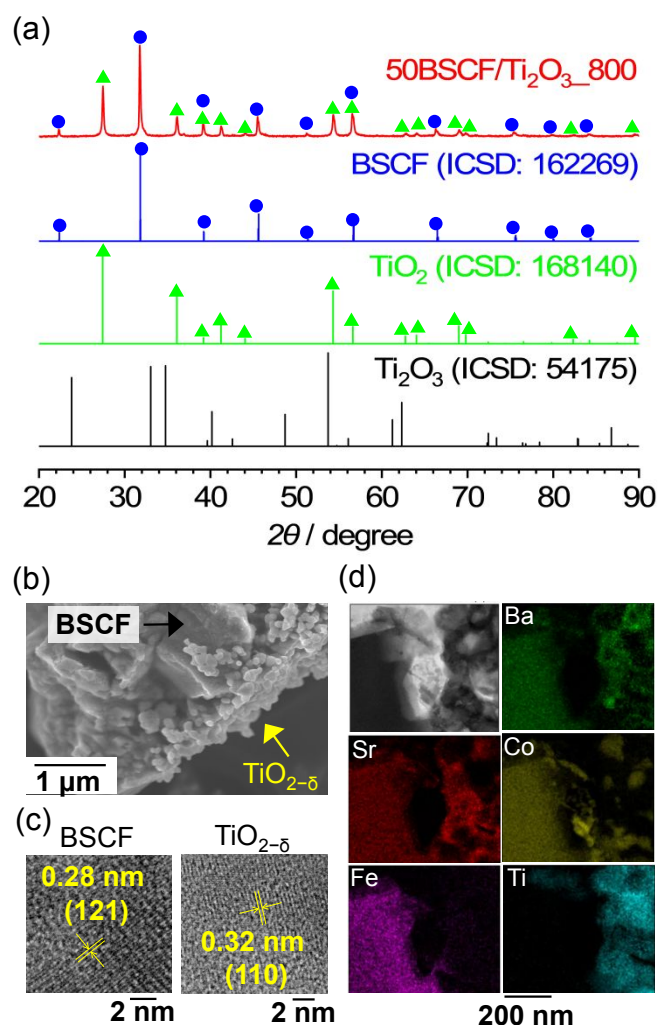

Fig. 2 (a) XRD patterns of (red) 50BSCF/Ti_2O_3_80, (blue) theoretical orthorhombic BSCF (ICSD: 161169), (green) theoretical tetragonal rutile-type TiO_2 (ICSD: 168140) and (black) theoretical Ti_2O_3 (ICSD: 54175). (b) SEM image of 50BSCF/Ti_2O_3_800. (c) HR-TEM images of 50BSCF/Ti_2O_3_800, which highlight the fringes of BSCF and $TiO_{2-\delta}$ crystals. (d) STEM-EDX images of the cross-section of 50BSCF/Ti_2O_3_800.

curves indicate that BSCF_800 generated only a slight OER current. This is due to the absence of a conductive support in the catalyst layer, which inhibits the electron transport from the active sites on BSCF to the electrode because of the low conductivity of BSCF, as shown in Table S1. Additionally, Ti_2O_3_800 did not cause any OER current because Ti_2O_3 did not intrinsically catalyze OER. However, 50BSCF/Ti_2O_3_800 generated a much higher OER current than BSCF_800 and Ti_2O_3_800 because the conductive titanium oxide support can promote electron transport to the electrode. Furthermore, notably, 50BSCF/Ti_2O_3_800 exhibited a larger OER current than 50BSCF/Ti_2O_3_PM. It is attributed that the process of physical mixing resulted in larger grain boundary resistance among BSCF and Ti_2O_3 particles than after annealing, and the consequent bulk conductivity remained low, as exhibited in Table S1. However, the annealing at 800 °C induced superior bulk conductivity, which can facilitate electron transport in the catalyst layer on RDE, which leads to the considerably enhanced OER current of 50BSCF/Ti_2O_3_800. Thus, annealing was necessary for the fabrication of efficient electrodes that are made of BSCF and conductive Ti_2O_3.

Furthermore, the OER polarization curves for 50BSCF/Ti_2O_3_200, 400, 600, and 800 are shown in Fig. 3b, which demonstrates that higher annealing temperature resulted in higher OER current. To understand the effect of annealing temperature, we measured the electrical conductivity of bulk samples, and the results are shown in Table S1. The conductivities were positively correlated with annealing temperature, i.e., higher annealing temperature resulted in higher conductivity. This is due to the reduction of grain boundary resistance at higher annealing temperature,[30] which enhances the electron transfer between BSCF and $TiO_{2-\delta}$ particles. Additionally, we examined the effect of the weight composition of BSCF. Several BSCF/Ti_2O_3 samples with the BSCF composition of 10, 30, 50, 70, and 90 wt% were fabricated by annealing at 800 °C and are denoted as 10BSCF/Ti_2O_3_800, 30BSCF/Ti_2O_3_800, 50BSCF/Ti_2O_3_800, 70BSCF/Ti_2O_3_800, and 90BSCF/Ti_2O_3_800, respectively. The XRD patterns and bulk conductivities of the samples are shown in Fig. S9 and Table S1, respectively. Their OER polarization curves are shown in Fig. 3c and were used to calculate the OER mass activity by normalizing the OER current at 1.63 V with the loaded amount of BSCF on RDE. Fig. 3d shows the OER mass activity, which indicates that 50BSCF/Ti_2O_3_800 possesses the highest mass activity. This can be explained as a trade-off between the number of accessible OER active sites and the conductivity of BSCF/Ti_2O_3. In the case of lower BSCF compositions, i.e., 10 and 30 wt%, their bulk conductivities were the same as that of the 50 wt% sample, as shown in Table S1, whereas the considerable number of OER active sites on the BSCF surface was covered by $TiO_{2-\delta}$, which inhibited catalytic OER. Therefore, their OER mass activity was inferior to that of the 50 wt% sample. In contrast, for higher BSCF compositions, i.e., 70 and 90 wt%, the samples contained more accessible OER active sites, whereas the bulk conductivities were diminished because of the insufficient amount of $TiO_{2-\delta}$, as shown in Table S1, which prevented efficient electron transport from active sites to the electrode and decreased the mass activity. Therefore, 50 wt% BSCF is the optimal composition for the mass activity.

Finally, we tested the durability of BSCF/Ti_2O_3 in the OER process to demonstrate the durability of the Ti_2O_3 support at high potential conditions. 50BSCF/Ti_2O_3_800, which is the optimized sample, was chosen to evaluate durability by repeated potential cycles in the OER region, and the results were compared with those of a conventional carbon support, CNT, which is denoted as BSCF/CNT. Fig. 4a shows the initial and 2000th OER polarization curves of 50BSCF/Ti_2O_3_800, which demonstrate a considerably stable OER performance without current loss after 2000 cycles. Conversely, Fig. 4b shows the initial and 2000th OER polarization curves of BSCF/CNT, and its OER current dramatically decreased after 2000 cycles because of carbon corrosion at high potential. Fig. 4c shows a change in the OER overpotentials of 50BSCF/Ti_2O_3_800 and BSCF/CNT as a function of cycle number. The OER overpotential is defined as the potential difference between the theoretical (1.23 V vs. RHE) and actual potential, when reaching the current density of 10 mA cm$^{-2}_{disk}$. The overpotential in BSCF/CNT rapidly increased with an increase in the number of cycles, whereas 50BSCF/Ti_2O_3_800 retained well its overpotential, which is ascribed to the high stability of titanium oxide at high potential. Furthermore, we characterized the morphology and elemental composition of 50BSCF/Ti_2O_3_800 after the durability test. Fig. 4d shows the TEM images of $TiO_{2-\delta}$ particles before and after 2000 cycles. The TEM observation confirmed that the particle morphology of $TiO_{2-\delta}$ was unchanged after 2000 cycles.
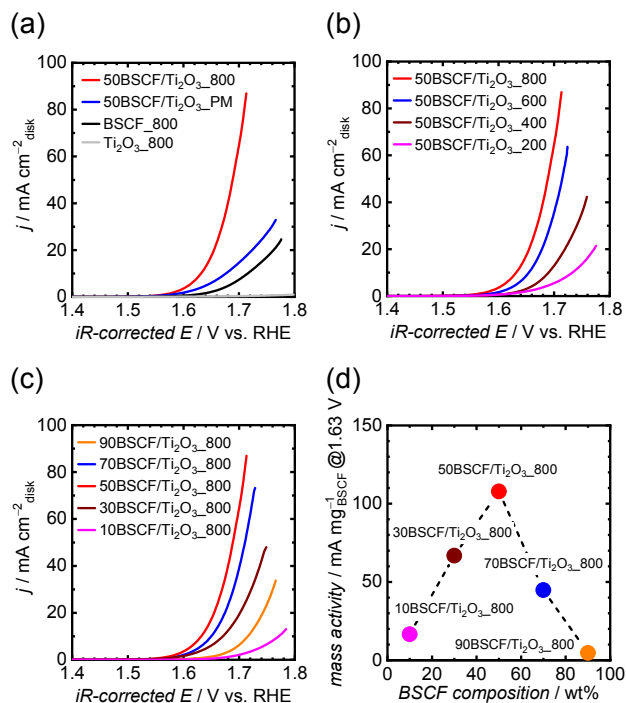
Fig. 3 OER activities of BSCF/Ti_2O_3 in O_2-saturated 1 M KOH. (a) OER polarization curves of 50BSCF/Ti_2O_3_800, 50BSCF/Ti_2O_3_PM, BSCF_800, and Ti_2O_3_800. The graph shows the 10th cycle of the reverse scan sweeps between 1.2 and 1.8 V (RHE). (b) OER polarization curves of BSCF/Ti_2O_3, which were fabricated at different annealing temperatures. (c) OER polarization curves of BSCF/Ti_2O_3 bearing different BSCF compositions. (d) OER mass activities of BSCF/Ti_2O_3 with different BSCF compositions.

COMMUNICATION

Journal Name
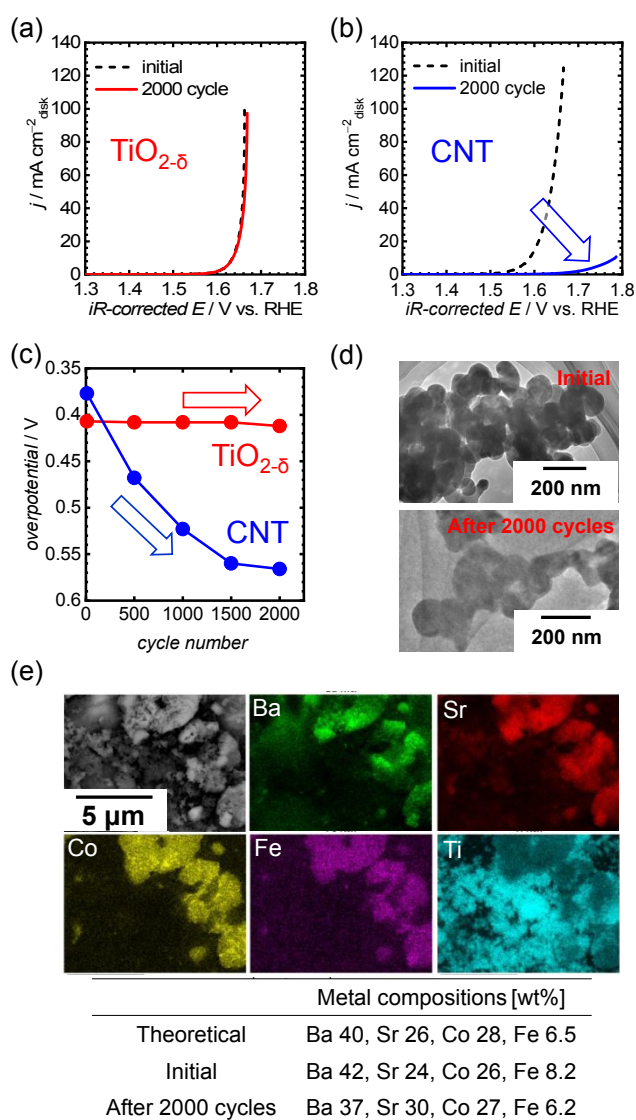
Fig. 4 Results of durability tests of BSCF/Ti$_2$O$_3$ and BSCF/CNT. (a) OER polarization curves of initial 50BSCF/Ti$_2$O$_3$_800 and after 2000 cycles in O$_2$-saturated 1 M KOH. (b) OER polarization curves of initial BSCF/CNT and after 2000 cycles in O$_2$-saturated 1 M KOH. (c) Change in the overpotential of 50BSCF/Ti$_2$O$_3$_800 and BSCF/CNT as a function of cycle number. (d) TEM images of TiO$_{2-\delta}$ particles before and after 2000 cycles. (e) SEM-EDX images of 50BSCF/Ti$_2$O$_3$_800 after 2000 cycles and quantified metal components in the initial BSCF particles as well as those after 2000 cycles.

doped tin oxide and molybdenum oxide.[31,32] Thus, Ti$_2$O$_3$ support is promising as a conductive support for electrochemical catalytic reactions at high potential conditions.

Conclusions

We applied Ti$_2$O$_3$ as a highly durable catalyst support for electrocatalytic reactions at high potential conditions. The model OER electrocatalyst/conductive support sample, *i.e.*, BSCF/Ti$_2$O$_3$, demonstrated excellent corrosion resistance to high potential. BSCF/Ti$_2$O$_3$ completely retained its OER performance after 2000 repeated potential cycles, which indicated that it had a much better durability during the OER process than the CNT support. Thus, Ti$_2$O$_3$ is promising as a conductive support for electrochemical catalytic reactions at high potential conditions.

Conflicts of interest

There are no conflicts to declare.

Acknowledgments

However, for BSCF/CNT, the tubular structure of CNT did not remain and was agglomerated after 2000 cycles, as shown in Fig. S10, which indicated carbon corrosion by repeated potential cycles at high potential. Furthermore, Figure 4e shows SEM-EDX images of 50BSCF/Ti$_2$O$_3$_800 after 2000 cycles, which indicate that BSCF and TiO$_{2-\delta}$ still existed separately. Additionally, the metal components in BSCF and TiO$_{2-\delta}$ remained during the repeated potential cycles in the OER region, and BSCF retained the compositions of Ba, Sr, Co, and Fe after 2000 cycles. These results demonstrated that the TiO$_{2-\delta}$ support, which was transformed from Ti$_2$O$_3$ during annealing, was more durable than the CNT support for long-term OER performance. Furthermore, the TiO$_{2-\delta}$ support was retained under the harsher potential conditions than those for previously reported metal oxide supports, such as antimony-

Notes and references

1 J. G. Bednorz and K. A. Muller, *Z. Phys. B-Condens. Mat.*, 1986, **64**, 189–193.
2 K. Takada, H. Sakurai, E. Takayama-Muromachi, F. Izumi, R. A. Dilanian and T. Sasaki, *Nature*, 2003, **422**, 53–55.
3 Y. Kamihara, T. Watanabe, M. Hirano and H. Hosono, *J. Am. Chem. Soc.*, 2008, **130**, 3296–3297.
4 N. Vlachopoulos, P. Liska, J. Augustynski and M. Gratzel, *J. Am. Chem. Soc.*, 1988, **110**, 1216–1220.
5 M. Gratzel, *Inorg. Chem.*, 2005, **44**, 6841–6851.
6 Y. Kato and T. Takei, *J.Inst. Electr. Eng. Jpn.*, 1933, **53**, 408–412.
7 L. Neel, *Ann. Phys.-Paris*, 1948, **3**, 137–198.
8 J. Suntivich, K. J. May, H. A. Gasteiger, J. B. Goodenough and Y. Shao-Horn, *Science*, 2011, **334**, 1383–1385.
9 Y. Y. Liang, Y. G. Li, H. L. Wang, J. G. Zhou, J. Wang, T. Regier and H. J. Dai, *Nat. Mater.*, 2011, **10**, 780–786.
10 H. T. Kreissl, M. M. J. Li, Y. K. Peng, K. Nakagawa, T. J. N. Hooper, J. V. Hanna, A. Shepherd, T. S. Wu, Y. L. Soo and S. C. E. Tsang, *J. Am. Chem. Soc.*, 2017, **139**, 12670–12680.
11 S. Shibata, K. Sugahara, K. Kamata and M. Hara, *Chem. Commun.*, 2018, **54**, 6772–6775.
12 Y. Sugawara, K. Kamata and T. Yamaguchi, *ACS Appl. Energy Mater.*, 2019, **2**, 956–960.
13 E. Hayashi, Y. Yamaguchi, K. Kamata, N. Tsunoda, Y. Kumagai, F. Oba and M. Hara, *J. Am. Chem. Soc.*, 2019, **141**, 890–900.
14 E. Antolini, *Appl. Catal. B-Environ.*, 2009, **88**, 1–24.
15 Y. L. Zhu, W. Zhou and Z. P. Shao, *Small*, 2017, **13**, 1603793.

COMMUNICATION

16 Y. Sugita, T. Tamaki, H. Kuroki and T. Yamaguchi, *Nanoscale Adv.*, 2020, **2**, 171–175.

17 K. Kinoshita, *Carbon: Electrochemical and Physicochemical Properties*, John Wiley & Sons, New York, 1988.

18 T. Ioroi, H. Senoh, S. I. Yamazaki, Z. Siroma, N. Fujiwara and K. Yasuda, *J. Electrochem. Soc.*, 2008, **155**, B321–B326.

19 S. Y. Huang, P. Ganesan, S. Park and B. N. Popov, *J. Am. Chem. Soc.*, 2009, **131**, 13898–13899.

20 K. Kakinuma, M. Uchida, T. Kamino, H. Uchida and M. Watanabe, *Electrochim. Acta*, 2011, **56**, 2881–2887.

21 Y. Z. Lu, Y. Y. Jiang, X. H. Gao, X. D. Wang and W. Chen, *J. Am. Chem. Soc.*, 2014, **136**, 11687-11697.

22 J. M. Honig and T. B. Reed, *Phys. Rev.*, 1968, **174**, 1020–1026.

23 P. G. Wahlbeck and P. W. Gilles, *J. Am. Ceram. Soc.*, 1966, **49**, 180–183.

24 T. Arai, O. Takashi, K. Amemiya and T. Takahashi, *SAE Int. J. Alt. Power.*, 2017, **6**, 145–150.

25 C. Cai, Y. Rao, J. F. Zhou, L. C. Zhang, W. Chen, Z. H. Wan, J. T. Tan and M. Pan, *J. Power Sources*, 2020, **473**, 7.

26 K. Sugahara, K. Kamata, S. Muratsugu and M. Hara, *ACS Omega*, 2017, **2**, 1608–1616.

27 T. Itoh, Y. Nishida, A. Tomita, Y. Fujie, N. Kitamura, Y. Idemoto, K. Osaka, I. Hirosawa and N. Igawa, *Solid State Commun.*, 2009, **149**, 41–44.

28 L. D. Li, J. Q. Yan, T. Wang, Z. J. Zhao, J. Zhang, J. L. Gong and N. J. Guan, *Nat. Commun.*, 2015, **6**, 10.

29 B. Q. Xu, H. Y. Sohn, Y. Mohassab and Y. P. Lan, *RSC Adv.*, 2016, **6**, 79706–79722.

30 R. Lahouli, J. Massoudi, M. Smari, H. Rahmouni, K. Khirouni, E. Dhahri and L. Bessais, *RSC Adv.*, 2019, **9**, 19949–19964.

31 H. S. Oh, H. N. Nong, T. Reier, A. Bergmann, M. Gliech, J. F. de Araujo, E. Willinger, R. Schlogl, D. Teschner and P. Strasser, *J. Am. Chem. Soc.*, 2016, **138**, 12552–12563.

32 M. Tariq, W. Q. Zaman, W. Sun, Z. H. Zhou, Y. Y. Wu, L. M. Cao and J. Yang, *ACS Sustainable Chem. Eng.*, 2018, **6**, 4854–4862.